





Critical properties of calibrated relativistic mean-field models for the transition to warm, nonhomogeneous nuclear and stellar matter

Olfa Boukari ¹, Helena Pais ², Sofija Antić ³, and Constança Providência ²

¹*ISEPBG-Soukra, University of Carthage, Avenue de la République BP 77-1054 Amilcar, Tunisia*

²*CFisUC, Department of Physics, University of Coimbra, 3004-516 Coimbra, Portugal*

³*CSSM and CoEPP, School of Physical Sciences, University of Adelaide, Adelaide SA 5005, Australia*



(Received 16 July 2020; revised 15 December 2020; accepted 15 March 2021; published 10 May 2021)

The critical properties for the transition to warm, asymmetric, nonhomogeneous nuclear matter are analyzed within a thermodynamical spinodal approach for a set of well-calibrated equations of state. It is shown that even though different equations of state are constrained by the same experimental, theoretical, and observational data, and the properties of symmetric nuclear matter are similar within the models, the properties of very asymmetric nuclear matter, such as the one found inside of neutron stars, differ a lot for various models. Some models predict larger transition densities to homogeneous matter for β -equilibrated matter than for symmetric nuclear matter. Since one expects that such properties have a noticeable impact on the evolution of either a supernova or neutron star merger, this different behavior should be understood in more detail.

DOI: [10.1103/PhysRevC.103.055804](https://doi.org/10.1103/PhysRevC.103.055804)

I. INTRODUCTION

Core-collapse supernovae (CCSN) and neutron star (NS) mergers are two astrophysical explosive events where matter can reach temperatures above ≈ 50 MeV. In CCSN matter, β -equilibrium is not immediately reached, and a fixed proton fraction in the range of $0 < y_p < 0.6$ is usually considered in the simulations [1]. In these very energetic events, light and heavy nuclear clusters are supposed to form, guiding the neutrino dynamics, and affecting, for example, the cooling of the protoneutron star [2], or the disk dissolution of a NS merger [3–5]. Hence, it is extremely important for these clusters to be included in the equations of state (EoS) for CCSN and NS mergers simulations, and to determine under which temperature, density, and proton fraction matter will be clusterized.

At subsaturation densities, nuclear matter goes through a liquid-gas phase transition [6]. The border between the stable and unstable matter is denoted by spinodal [7], and it can be estimated via dynamical or thermodynamical calculations. In the first case, the instabilities are determined from the fluctuations around equilibrium. The zero-frequency one defines the spinodal surface. In this approach, both the presence of electrons and the Coulomb field can be taken into account. In the thermodynamical case, the region of instabilities is identified by the negative curvature of the free energy density, and the spinodal border is defined by a zero curvature. Considering a calculation that does not include the electron contribution and does not take into account the Coulomb interaction, the dynamical spinodal coincides with the thermodynamical spinodal in the infinite wave length limit. In the limit of small wavelengths, smaller than the nuclear force range, the instability region defined by the dynamical spinodal disappears. This

same small wavelength limit is obtained in a calculation of the dynamical spinodal that includes the electron contribution and the Coulomb interaction.

While the dynamical spinodal may give more realistic predictions for the crust-core phase transition in neutron stars because it allows us to take into account the finite-range effects of the nuclear force and the Coulomb interaction, the thermodynamic spinodal still gives a good estimation, as shown in Refs. [8–10]. In particular, in Ref. [10], the authors compared the nonhomogeneous to homogeneous matter transition density obtained within the thermodynamical and dynamical spinodals, and a more realistic approach, a Thomas-Fermi (TF) calculation of nonhomogeneous matter. Taking the TF calculation as reference, it was shown that, for β -equilibrium matter, the dynamical spinodal gives results comparable with TF, and the thermodynamical spinodal gives slightly larger ($\approx 10\%$) transition densities, [8]. Besides, for matter with a proton fraction equal to 0.3, as found in CCSN matter, the thermodynamical spinodal predicts transition densities close to the ones of a TF calculation. The liquid-gas phase transition calculated from the spinodal decomposition has been used in experiments to study the fragmentation of nuclear systems, in particular the time evolution of a compound nucleus during heavy-ion collisions [11].

The liquid-gas phase transition also occurs in stellar matter, and that explains why at subsaturation densities, one should expect clusterized matter in core-collapse supernovae, neutron star mergers, and the inner crust of neutron stars. Light and heavy clusters should form at subsaturation densities, which in cold catalyzed neutron stars correspond to the inner crust region [12]. In this case, spherical clusters form in the upper layers of the inner crust and in the bottom layers close to the crust-core transition, clusters with other geometries called

pasta phases may arise due to a competition between the Coulomb interaction and the nuclear force [13].

Calculations seem to indicate that heavy clusters, including spherical clusters and pasta phases, may exist well above 1 MeV, as shown in studies that consider a molecular dynamical description [14], a statistical description [15,16], or a single nucleus approximation [12,17–19]. Moreover, at finite temperatures, one expects that light clusters, which may be understood as few-nucleon correlations, dominate at low densities. At larger densities, but still below saturation density, light and heavy clusters coexist [20]. The existence of clustered matter is influenced by the temperature and proton fraction, and depends on the isovector properties of the nuclear matter model. Nonhomogeneous matter is expected below the critical end point of the nuclear liquid-gas phase transition, i.e., for a temperature of the order of 14–17 MeV [21].

Light clusters at low densities can be introduced as independent degrees of freedom within a generalized relativistic mean-field (RMF) approach [22–24]. The calibration of the couplings of these clusters has been performed by reproducing the equilibrium constants extracted from heavy ion collisions (HIC) [22,25,26]. In particular, it has been shown that it is important to take into account in medium effects when extracting the equilibrium constants from the experimental measurements [22]. Taking the parametrizations calibrated to the INDRA measurements [22], we have shown that the fraction of light clusters predicted up to the densities tested by INDRA are similar for different models. However, different models predict different dissolution densities [27].

In Ref. [28], a general approach to study the liquid-gas phase transition in asymmetric nuclear matter has been proposed within RMF models. The region of instability was identified by the negative curvature of the free energy. The approach allowed us to analyze the so-called distillation effect discussed in Refs. [7,11], which is occurring in asymmetric nuclear matter at the phase transition. In fact, the symmetry energy favors the formation of a quite symmetric liquid phase, while the gas phase stays very neutron rich. In Ref. [28] it was discussed that the strength of the distillation effect is model dependent and, in particular, density-dependent models show a weaker effect with respect to models with constant coupling constants. In Ref. [28], however, a very restricted number of models was analyzed.

Applying the same approach, in Ref. [9], a comparison of the behavior of two types of phenomenological nuclear models, the nonrelativistic Skyrme models and the RMF models, was performed. These two sets of models showed similar trends, although an anomalous behavior was obtained for one of the Skyrme models, the SIII model [29]. In this model, the spinodal has a convex behavior at the upper spinodal border of symmetric matter, which we will refer in the discussion as ρ_{sym} . As a consequence, for the SIII model, the transition from nonhomogeneous matter to homogeneous matter occurs at a larger density for neutron-rich matter than for symmetric matter, a behavior that none of the other models tested in that work showed. One of the characteristics of this model was its very small symmetry energy slope at saturation, ≈ 10 MeV.

The same formalism was applied more recently to analyze the effect of the density dependence of the symmetry energy

on the instability region [30]. In this work, the thermodynamical instabilities were calculated for hot asymmetric nuclear matter described by different RMF models. The goal was to perform a more systematic study, and to determine the critical densities and proton fractions, in order to understand how sensitive these properties are to the density dependence of the symmetry energy, and in particular, to its slope at saturation density. In fact, presently there are strong constraints on the symmetry energy, both from the experimental side [31] and from *ab initio* calculations for neutron matter that did not exist when the studies [9,28] were performed.

Present simulations of CCSN or neutron star mergers are performed taking into account realistic EoS, see, for instance, Refs. [32–34]. While the EoS chosen are generally calibrated at $T = 0$ MeV, it is important to understand their behavior under the extreme conditions attained in the above scenarios, in order to properly discuss the results of the simulations. It is the main objective of the present study to calculate the thermodynamic instabilities of several recently proposed RMF models in order to compare their finite-temperature behavior, and, therefore, to determine the finite temperature properties of nuclear models that have been calibrated at $T = 0$ MeV. As discussed in Ref. [10] the determination of the thermodynamical spinodal allows for a good estimation of the nonhomogeneous nuclear matter inside a neutron star or a CCSN while being numerically less demanding.

The following nuclear RMF models will be considered: SFHo and SFHx [33], FSU2R and FSU2H proposed in Refs. [35,36], TM1 [37], and the recently proposed TM1e [19,38], DD2 [24] and DDME2 [39], and finally, D1 and D2 [40], closely related to DD2. The main conclusion of the present work is that while calibrated models behave in a very similar way at zero temperature and symmetric matter, large differences were identified for both the critical temperatures and densities of β -equilibrated matter in very asymmetric matter. In some models, like SFHo and SFHx, the onset of homogeneous matter in β -equilibrated matter occurs at similar or larger densities than the ones found for symmetric nuclear matter. This will have consequences on the predictions of CCSN or NS merger simulations.

The structure of the paper is the following: in Sec. II, the general formalism of RMF models and spinodal calculation are briefly introduced; Sec. III discusses and compares the results on critical points, transition densities, and distillation effect between different models; and, finally, in Sec. IV, a few conclusions are drawn.

II. FORMALISM

A brief summary of the RMF formalism is given in the first part of the section, and we follow the notation previously used, see, e.g., Ref. [30], while the thermodynamical spinodal calculation and respective critical points are addressed in the Sec. II B.

A. Field theoretical models with RMF Lagrangian

In our set of RMF models, the nucleons, with mass M , interact with the scalar-isoscalar meson field σ with mass

m_σ , the vector-isoscalar meson field ω^μ with mass m_ω , and the vector-isovector meson field ρ^μ with mass m_ρ . The Lagrangian density is given by:

$$\mathcal{L} = \sum_{i=p,n} \mathcal{L}_i + \mathcal{L}_\sigma + \mathcal{L}_\omega + \mathcal{L}_\rho + \mathcal{L}_{\sigma\omega\rho}, \quad (1)$$

where the nucleon Lagrangian reads

$$\mathcal{L}_i = \bar{\psi}_i[\gamma_\mu iD^\mu - M^*]\psi_i, \quad (2)$$

with

$$iD^\mu = i\partial^\mu - g_\omega\omega^\mu - \frac{g_\rho}{2}\boldsymbol{\tau} \cdot \boldsymbol{\rho}^\mu. \quad (3)$$

The Dirac effective mass is given by

$$M^* = M - g_\sigma\sigma. \quad (4)$$

In the above equations, g_σ , g_ω , and g_ρ are the meson-nucleon couplings, and $\boldsymbol{\tau}$ are the SU(2) isospin matrices.

The mesonic Lagrangians are

$$\begin{aligned} \mathcal{L}_\sigma &= +\frac{1}{2}\left(\partial_\mu\phi\partial^\mu\sigma - m_\sigma^2\sigma^2 - \frac{1}{3}\kappa\sigma^3 - \frac{1}{12}\lambda\sigma^4\right), \\ \mathcal{L}_\omega &= -\frac{1}{4}\Omega_{\mu\nu}\Omega^{\mu\nu} + \frac{1}{2}m_\omega^2\omega_\mu\omega^\mu + \frac{\zeta}{4!}\zeta g_\omega^4(\omega_\mu\omega^\mu)^2, \\ \mathcal{L}_\rho &= -\frac{1}{4}\mathbf{B}_{\mu\nu} \cdot \mathbf{B}^{\mu\nu} + \frac{1}{2}m_\rho^2\rho_\mu \cdot \rho^\mu + \frac{\xi}{4!}g_\rho^4(\rho_\mu\rho^\mu)^2, \end{aligned} \quad (5)$$

where $\Omega_{\mu\nu} = \partial_\mu\omega_\nu - \partial_\nu\omega_\mu$, $\mathbf{B}_{\mu\nu} = \partial_\mu\boldsymbol{\rho}_\nu - \partial_\nu\boldsymbol{\rho}_\mu - g_\rho(\boldsymbol{\rho}_\mu \times \boldsymbol{\rho}_\nu)$, and κ , λ , ζ , and ξ are coupling constants.

The mesonic Lagrangian is supplemented with the following nonlinear term that mixes the σ , ω , and ρ mesons [33]:

$$\mathcal{L}_{\sigma\omega\rho} = g_\rho^2 f(\sigma, \omega_\mu\omega^\mu)\boldsymbol{\rho}^\mu \cdot \boldsymbol{\rho}_\mu. \quad (6)$$

For the SFHo and SFHx models, f is given by

$$f(\sigma, \omega_\mu\omega^\mu) = \sum_{i=1}^6 a_i\sigma^i + \sum_{j=1}^3 b_j(\omega_\mu\omega^\mu)^j, \quad (7)$$

while for the FSU2R, FSU2H, TM1, and TM1e models, this function f reduces to

$$f(\omega_\mu\omega^\mu) = \Lambda_v g_v^2 \omega_\mu\omega^\mu. \quad (8)$$

For these four models, the coupling constant of the nonlinear term ξ is absent.

For the density-dependent models, DD2, DDME2, and D1, the isoscalar couplings of the mesons i to the baryons are written in the following way, in terms of the baryonic density n_B :

$$g_i(n_B) = g_i(n_0)a_i \frac{1 + b_i(x + d_i)^2}{1 + c_i(x + d_i)^2}, \quad (9)$$

and the isovector ones are given by

$$g_i(n_B) = g_i(n_0) \exp[-a_i(x - 1)]. \quad (10)$$

Here, n_0 is the symmetric nuclear saturation density, and $x = n_B/n_0$. For the D2 model, there are additional terms in the vector density because of the energy-dependent self-energies, meaning that n_B and n_ω are no longer equal. For all density-dependent models, the coupling constants k , λ , ξ , and ζ are zero, together with the f function.

The energy density \mathcal{E} is given by:

$$\begin{aligned} \mathcal{E}^{NL} &= \sum_{i=p,n} E_i + \omega(\rho_p + \rho_n) + \rho_0(\rho_p - \rho_n) \\ &+ \frac{1}{2}m_\sigma^2\sigma^2 - \frac{1}{2}m_\omega^2\omega^2 - \frac{1}{2}m_\rho^2\rho_0^2 + \frac{\kappa}{6}\sigma^3 \\ &+ \frac{\lambda}{24}\sigma^4 - \frac{\zeta}{24}(g_\omega\omega)^4 - \frac{\xi}{24}(g_\rho\rho_0)^4 - g_\rho^2\rho_0^2 f, \end{aligned} \quad (11)$$

for the nonlinear (NL) models, which includes several nonlinear mesonic terms, and by

$$\mathcal{E}^{DD} = \sum_{i=p,n} E_i + \frac{1}{2}m_\sigma^2\sigma^2 - \frac{1}{2}m_\omega^2\omega^2 - \frac{1}{2}m_\rho^2\rho_0^2 - \Sigma_0^R n_B, \quad (12)$$

for the density-dependent (DD) models. Σ_0^R is the rearrangement term that appears only in the density-dependent models (see Refs. [24,39,40]), and is given by

$$\Sigma_0^R = \frac{\partial g_\omega}{\partial n_B} \omega n_B + \frac{\partial g_\rho}{\partial n_B} \rho_0(\rho_p - \rho_n)/2 - \frac{\partial g_\sigma}{\partial n_B} \sigma \rho_s. \quad (13)$$

In Eqs. (11) and (12), the single-particle energies E_i are given by

$$E_i = \frac{1}{\pi^2} \int dp p^2 \epsilon_i^*(f_{i+} + f_{i-}), \quad (14)$$

the nucleon number density is

$$\rho_i = \frac{1}{\pi^2} \int dp p^2 (f_{i+} - f_{i-}), \quad (15)$$

the scalar density is

$$\rho_s^i = \frac{1}{\pi^2} \int dp p^2 \frac{M^*}{\epsilon_i^*} (f_{i+} + f_{i-}), \quad (16)$$

the distribution functions are defined as

$$f_{i\pm} = \frac{1}{1 + \exp[(\epsilon_i^* \mp v_i)/T]}, \quad (17)$$

with $\epsilon_i^* = \sqrt{p^2 + M^{*2}}$, and the nucleons effective chemical potential as

$$v_i = \mu_i - g_\omega\omega - g_\rho t_{3i}\rho_0 - \Sigma_0^R, \quad (18)$$

where t_{3i} is the third component of the isospin operator, and the rearrangement term is included only for the DD models. The entropy density \mathcal{S} is calculated from

$$\begin{aligned} \mathcal{S} &= - \sum_{i=p,n} \int \frac{d^3p}{4\pi^3} [f_{i+} \ln f_{i+} + (1 - f_{i+}) \ln(1 - f_{i+}) \\ &+ (f_{i+} \leftrightarrow f_{i-})]. \end{aligned} \quad (19)$$

The free energy density \mathcal{F} is then obtained from the thermodynamic relation

$$\mathcal{F} = \mathcal{E} - T\mathcal{S}. \quad (20)$$

B. Stability conditions

In the present study, we determine the region of instability of nuclear matter constituted by protons and neutrons by calculating the spinodal surface in the (ρ_p, ρ_n, T) space.

Stability conditions for asymmetric matter impose that the curvature matrix of the free energy density [28]

$$C_{ij} = \left(\frac{\partial^2 \mathcal{F}}{\partial \rho_i \partial \rho_j} \right)_T, \quad (21)$$

or, equivalently,

$$C = \begin{pmatrix} \frac{\partial \mu_n}{\partial \rho_n} & \frac{\partial \mu_n}{\partial \rho_p} \\ \frac{\partial \mu_p}{\partial \rho_n} & \frac{\partial \mu_p}{\partial \rho_p} \end{pmatrix}, \quad (22)$$

is positive. The stability conditions impose $\text{Tr}(C) > 0$ and $\text{Det}(C) > 0$, which is equivalent to the requirement that the two eigenvalues

$$\lambda_{\pm} = \frac{1}{2}(\text{Tr}(C) \pm \sqrt{\text{Tr}(C)^2 - 4\text{Det}(C)}) \quad (23)$$

are positive. The largest eigenvalue, λ_+ , is always positive, and the instability region is delimited by the surface $\lambda_- = 0$. Interesting information is given by the associated eigenvectors $\delta\rho^{\pm}$, defined as

$$\frac{\delta\rho_p^{\pm}}{\delta\rho_n^{\pm}} = \frac{\lambda_{\pm} - \frac{\partial \mu_n}{\partial \rho_n}}{\frac{\partial \mu_n}{\partial \rho_p}}. \quad (24)$$

In particular, the eigenvector associated with the eigenvalue that defines the spinodal surface determines the instability direction, i.e., the direction along which the free energy decreases.

The critical points for different temperatures T , which are important for the definition of conditions under which the system is expected to clusterize, are also going to be calculated. These points satisfy simultaneously [28,41]

$$\text{Det}(C) = 0 \quad (25)$$

$$\text{Det}(\mathcal{M}) = 0, \quad (26)$$

with

$$\mathcal{M} = \begin{pmatrix} C_{11} & C_{12} \\ \frac{\partial |C|}{\partial \rho_p} & \frac{\partial |C|}{\partial \rho_n} \end{pmatrix}. \quad (27)$$

At a fixed temperature, the critical points, defined by the pairs

$$(\rho_{p,c}, \rho_{n,c}) \quad \text{or} \quad (\rho_c, y_{p,c}) \quad (28)$$

with

$$\rho_c = \rho_{p,c} + \rho_{n,c}, \quad y_{p,c} = \rho_{p,c} / \rho_c, \quad (29)$$

represent the points where the spinodal and the binodal are coincident, and correspond to the points of the spinodal section with maximum pressure (there are two pairs, which are symmetrical with respect to the $\rho_p = \rho_n$ line). For cold matter, the (ρ_p, ρ_n) line defined by the β -equilibrium condition crosses the spinodal very close to the $T = 0$ critical point, and, therefore, the crust-core transition density is well estimated from the crossing of the β -equilibrium (ρ_p, ρ_n) line and the spinodal section. The thermodynamical spinodals and respective critical points are going to be calculated for a series of the introduced RMF models in the next section.

TABLE I. The symmetric nuclear matter properties at saturation density for the models under study: the nuclear saturation density n_0 , the binding energy per particle B/A , the incompressibility K , the symmetry energy E_{sym} , the slope of the symmetry energy L , and the nucleon effective mass M^* . All quantities are in MeV, except for n_0 that is given in fm^{-3} , and the effective nucleon mass is normalized to the nucleon mass.

Model	n_0	B/A	K	E_{sym}	L	M^*/M
SFHo [33]	0.158	16.13	243	31.4	44	0.76
SFHx [33]	0.16	16.16	261	27	43	0.71
FSU2R [35,36]	0.15	16.28	238	30.7	47	0.59
FSU2H [35,36]	0.15	16.28	238	30.5	45	0.59
TM1 [37]	0.145	16.3	281	36.9	111	0.63
TM1e [19,38]	0.145	16.3	281	31.4	40	0.63
DDME2 [39]	0.152	16.14	251	32.3	51	0.57
DD2 [24]	0.149	16.02	243	31.7	58	0.56
D1 [40]	0.15	16.0	240	32.0	60	0.56
D2 [40]	0.146	16.0	240	32.0	60	0.56

III. RESULTS AND DISCUSSION

In this section, we start by elaborating in more detail on the models we use. For each of them, we calculate the thermodynamic instability regions, the critical points, the transition densities, and the isospin distillation effect for a given temperature. To conclude, a discussion of the results will be presented.

A. Models

In the present study we consider a set of RMF models calibrated to properties of nuclei and nuclear matter. These models fall into two different types: one with density-dependent couplings, DD2, DDME2, D1, and D2, which we designate by DD models, and the other with nonlinear couplings, SFHo, SFHx, FSU2R, FSU2H, TM1, and TM1e, which we designate by NL models. In Table I, some symmetric nuclear matter properties calculated at saturation density are given for all the models that we explore. The calculations performed in the present study for the SFHo and SFHx models used the parametrizations published in Ref. [33]. However, the reader should note that the values shown in this table for these models are not equal to the ones shown in Table 2 of Ref. [33] because the parametrizations published in Ref. [33] do not correspond to the last version these authors used in their work [42].

Concerning the NL models, SFHo and SFHx [33] include several nonlinear terms of higher order. They were constructed in such a way that they satisfy constraints coming from nuclear masses, giant monopole resonances, and binding energies and charge radii of ^{208}Pb and ^{90}Zr . Besides, they satisfy the $2M_{\odot}$ constraint [43], and the pressure of neutron matter is always positive and increasing.

FSU2H and FSU2R were calibrated in order to reproduce the properties of finite nuclei, constraints from kaon production and collective flow in HIC, and to predict neutron matter pressures consistent with effective chiral forces in Refs. [35,36]. Both models reproduce $2M_{\odot}$ stars, have a

symmetry energy and its slope at saturation consistent with current laboratory predictions, and their neutron skin thickness is compatible with several experiments, both for ^{208}Pb and for ^{48}Ca , as from measurements of the electric dipole polarizability of nuclei. The main difference between both is the softer symmetry energy of FSU2H, with a slope at saturation 5% smaller.

TM1e [19,38] accurately describes finite nuclei, gives two solar-mass neutron stars and radii compatible with the latest astrophysical observations by NICER [44]. Its symmetry energy and slope at saturation are also consistent with astrophysical observations and terrestrial nuclear experiments [1,45,46], while TM1 [37] fails these constraints, and, in particular, has a very large symmetry energy and slope at saturation.

With respect to the density-dependent models, D1 and D2 [40] are close to DD2 [24], which was fitted to properties of nuclei and reproduces $2M_{\odot}$ stars. D2 includes an energy dependence that was fitted to the optical potentials [47]. This model does not reach the two-solar-mass constraint since the EoS becomes very soft when the optical potential constraint is satisfied. DDME2 [39] was adjusted to reproduce the properties of symmetric and asymmetric nuclear matter, binding energies, charge radii, and neutron radii of spherical nuclei.

In order to better understand the isovector properties of these models besides their properties at saturation density, in Fig. 1 the symmetry energy (top panel), its slope (middle panel), and the neutron matter pressure (bottom panel) are plotted as a function of the baryonic density. In the bottom panel, we also include the 1σ constraint imposed on the pressure of neutron matter EoS by chiral effective field theoretical (χ EFT) calculations [48]. Some conclusions may be drawn: SFHo is the model that presents a softer symmetry energy above $\approx 0.5\rho_0$ and, even below this density, it is only SFHx that is slightly softer. While DDME2, DD2, SFHo, and SFHx are quite similar below $0.5\rho_0$, FSU2R, FSU2H, and TM1e are clearly stiffer in this range of densities. TM1 has an almost linear behavior with density, presenting the smallest values below $\approx 0.1\text{ fm}^{-3}$, and the largest above that value. In fact, above $\approx 0.1\text{ fm}^{-3}$, all models have a similar behavior except TM1 that is much stiffer, and SFHx that is quite soft.

Looking at the slope of symmetry energy, we see that TM1e, FSU2R, and FSU2H follow the same trend, though TM1e has the lowest L at saturation. TM1, on the other hand, is the only model that stands out, never coming below 100 MeV and having the steepest behavior for $\rho < 0.02\text{ fm}^{-3}$. SFHx has a similar behavior compared to the density-dependent models, while SFHo deviates slightly from this trend, showing a steeper behavior.

It is also quite instructive to analyze the behavior of the neutron matter pressure. As expected TM1 completely misses the behavior of the χ EFT EoS. However, the other models also present a quite diversified behavior. Density-dependent models are the ones that best satisfy the χ EFT constraints. SFHo also follows approximately the χ EFT EoS behavior. On the other hand, SFHx shows a quite low pressure in a considerable large range of densities, in particular, for $\rho \lesssim 0.06\text{ fm}^{-3}$. Finally, models TM1e, FSU2R, and FSU2H show a too soft behavior of the neutron matter pressure with density below

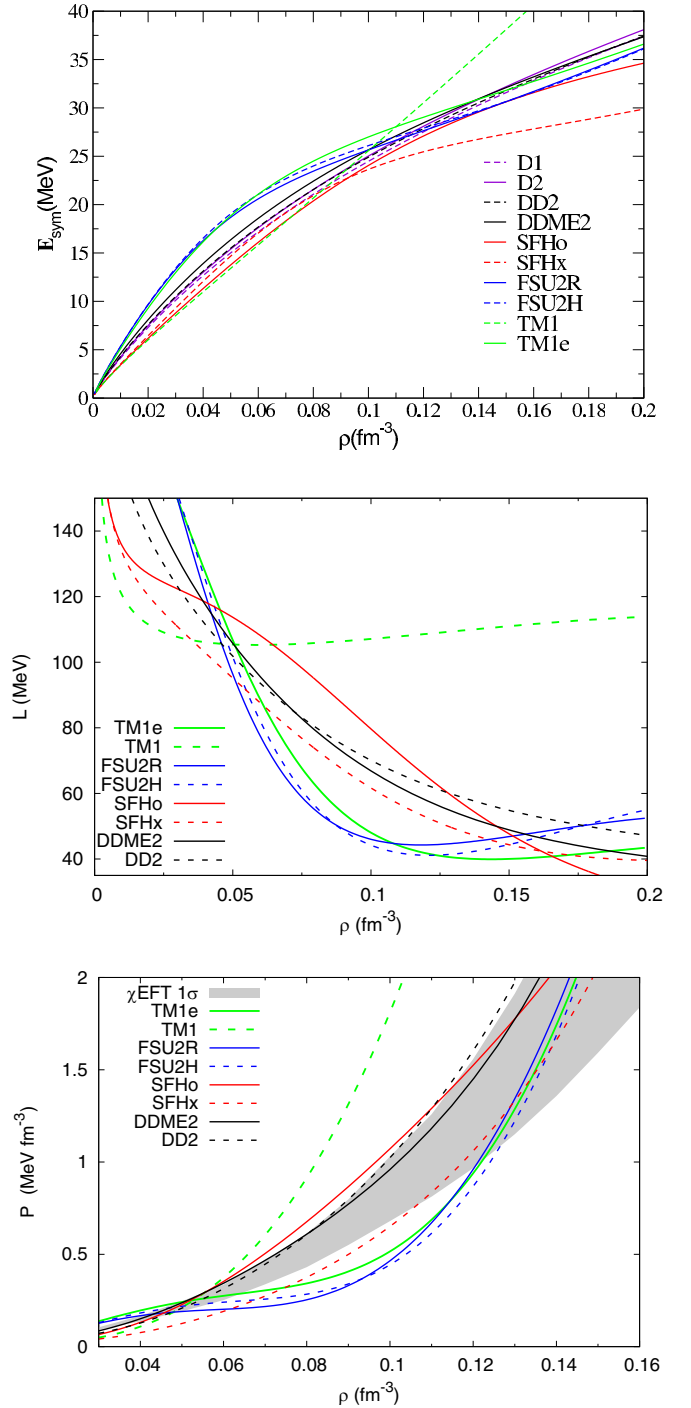


FIG. 1. The symmetry energy (top), the symmetry energy slope (middle), and the neutron matter pressure (bottom) as a function of the density for the models under consideration. The gray band in the bottom panel represents the 1σ constraint from chiral effective field theoretical calculations [48].

$\rho = 0.08\text{ fm}^{-3}$, more strongly the last two models: model FSU2R has an almost zero slope pressure at $\rho \approx 0.05\text{ fm}^{-3}$. Above $\rho = 0.1\text{ fm}^{-3}$, the pressure of these three models becomes too stiff. We will discuss how these behaviors reflect themselves on the instability regions.

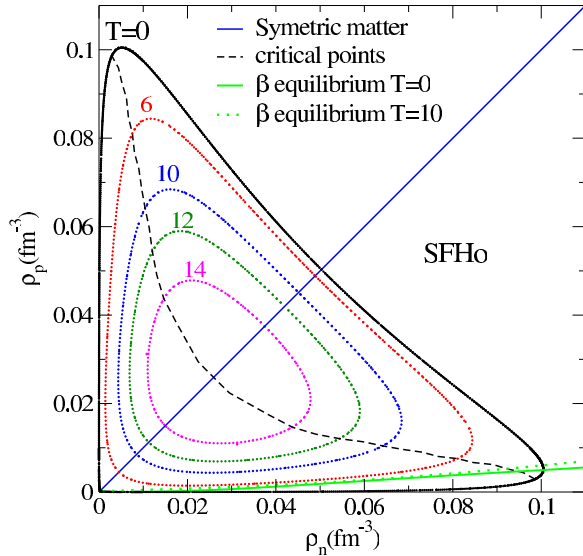


FIG. 2. The spinodal regions on the (ρ_n, ρ_p) plane for the SFHo model at $T = 0, 6, 10, 12,$ and 14 MeV. Also shown are the β -equilibrium EoS at $T = 0$ (green solid) and 10 MeV (green dashed), the critical points line (black dashed), and the symmetric matter line (blue solid).

B. Spinodal sections and critical points

In Fig. 2, we show the spinodal sections obtained with the SFHo model at different temperatures, imposing $\lambda_- = 0$, defined in Eq. (23). The larger the temperature, the smaller the section, which will be eventually reduced to a point at the critical temperature, that corresponds to the critical end point (CEP), and occurs for symmetric matter. For SFHo, the CEP occurs at $T = 16.14$ MeV and $\rho = 0.051$ fm^{-3} . It is interesting to notice that the $T = 0$ spinodal is convex at the $\rho_p = \rho_n$ point. Many of the models previously studied are concave at this point, see for instance Ref. [9] for a discussion. In Ref. [9], only the model SIII [49] shows a quite abnormal behavior. A consequence of this behavior is the prediction that highly asymmetric matter is still nonhomogeneous at densities close, or even above, the transition density from nonhomogeneous to homogeneous matter of symmetric matter, designated in the following as ρ_{sym} . However, one would expect that the contribution of the repulsive symmetry term to the binding energy of nuclear matter would move the transition density to lower densities, as the proton-neutron asymmetry increases.

In the same figure, the EoS for β -equilibrium matter calculated at two different temperatures, $T = 0$ and 10 MeV, is also represented. The crust-core transition density at a given temperature may be estimated from the intersection of the EoS with the spinodal at that same temperature. In Refs. [8,10], it was shown that this is a good estimation although slightly larger than the values obtained within a Thomas-Fermi or a dynamical spinodal calculations. For the two temperatures shown, we conclude that: (i) the $T = 0$ MeV EoS intercepts the $T = 0$ spinodal at $\rho_t = 0.105$ fm^{-3} , indicating that the crust of a neutron star described by this model extends until approximately this density. The line $y_p = 0.5$ intercepts the spinodal at $\rho_{\text{sym}} = 0.101$ fm^{-3} , a density slightly smaller than ρ_t ; (ii) the $T = 10$ MeV EoS does not intercept the respective

TABLE II. The transition density ρ_t , the correspondent proton fraction y_{p_t} , and the density of symmetric matter ρ_{sym} , obtained at $T = 0$ MeV for some of the models considered in this work.

Model	ρ_t (fm^{-3})	y_{p_t}	ρ_{sym} (fm^{-3})
SFHx	0.122	0.041	0.103
SFHo	0.105	0.047	0.101
FSU2R	0.087	0.045	0.095
FSU2H	0.092	0.046	0.095
TM1e	0.094	0.050	0.094
TM1	0.047	0.025	0.070
DD2	0.081	0.034	0.095
D1	0.082	0.032	0.102
DDME2	0.087	0.039	0.099

spinodal, and this indicates that β -equilibrium matter at this temperature is homogeneous.

The line of critical points is also displayed in the figure. At a given temperature, these are the two points in the spinodal section that have maximum pressure, and where the direction of the instability is parallel to the tangent to the spinodal. This means that the pressure above P_{max} belongs to the homogeneous matter phase.

In Table II, the transition density of both β -equilibrium matter ρ_t , and of symmetric matter, ρ_{sym} , are given, together with the proton fraction at the β -equilibrium transition for each model. For β -equilibrium matter, the transition occurs for $y_p \ll 0.5$. All models have $\rho_{\text{sym}} > \rho_t$, except TM1e, SFHo, and SFHx, the last model having an extreme transition density of ≈ 0.12 fm^{-3} . For TM1e, both densities are equal. SFHo and SFHx are also the models that predict larger crust-core transition densities.

The spinodal sections obtained at different temperatures for the NL models we consider in this study are plotted in Figs. 3 and 4. SFHo and SFHx present a convex curvature at the transition density of symmetric matter. However, one would expect that more neutron-rich matter would have a smaller unstable density range. The convex behavior occurs for low temperatures and it will have no astrophysical consequences because for these temperatures stellar matter is very neutron rich. However, it could have some noticeable effect in multifragmentation heavy-ion collisions with symmetric systems entering into multifragmentation at lower densities. They also have a bigger instability region as compared to the other models. Comparing TM1 and TM1e, it is clearly seen that the ones with a smaller slope L at saturation have spinodal sections that extend to more asymmetric matter, as discussed in Ref. [8], right up to almost the CEP, which occurs for symmetric nuclear matter. This implies that in warm stellar matter in β equilibrium, as the one found in neutron star mergers, finite clusters will appear at larger temperatures and proton asymmetries, having direct implications in processes such as neutrino cross sections.

On the other hand, the spinodals for DD models, which are plotted in Fig. 5, show a behavior closer to the one presented by TM1, although having a much smaller slope L : the spinodal sections are smaller, do not extend to so asymmetric nuclear matter, and they are all concave at $y_p = 0.5$.

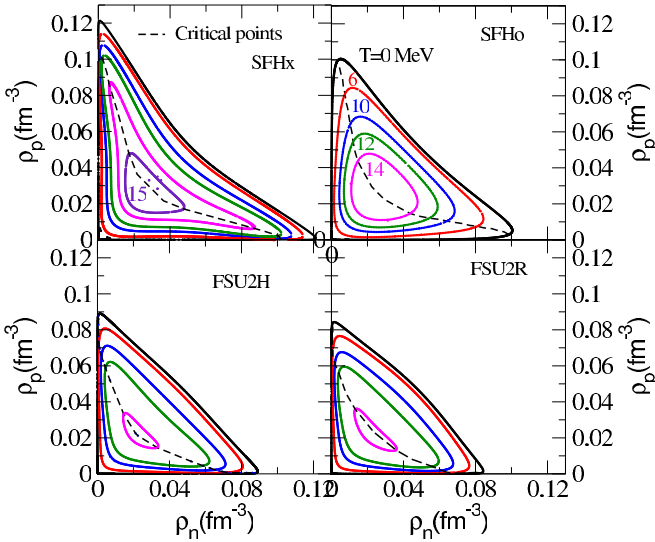


FIG. 3. The spinodal sections on the (ρ_n, ρ_p) plane for SFHx (top left), SFHo (top right), FSU2H (bottom left), and FSU2R (bottom right) at $T = 0, 6, 10, 12,$ and 14 MeV. The SFHx model is the only one that presents an unstable region at $T = 15$ MeV. The critical points line is given by the black dashed line.

The differences between the NL and DD spinodals are also clearly seen by comparing the critical point properties at each temperature. In Table III, we show, for several temperatures, the critical densities and correspondent proton fractions. The

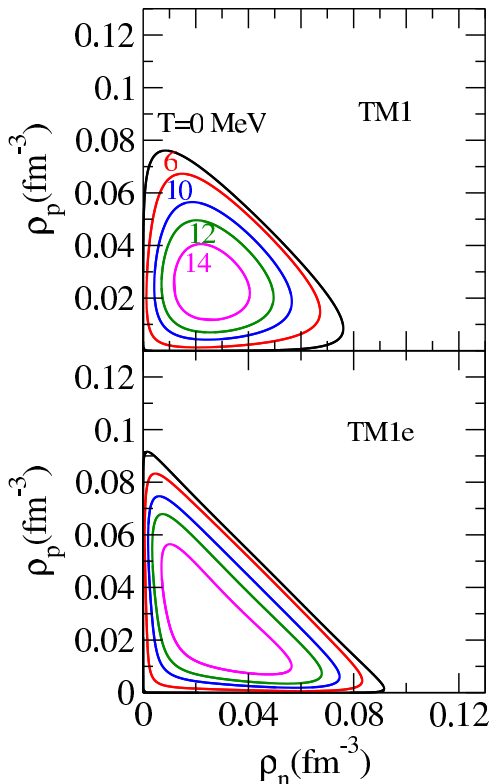


FIG. 4. The spinodal sections on the (ρ_n, ρ_p) plane for TM1 (top) and TM1e (bottom), at $T = 0, 6, 10, 12,$ and 14 MeV.

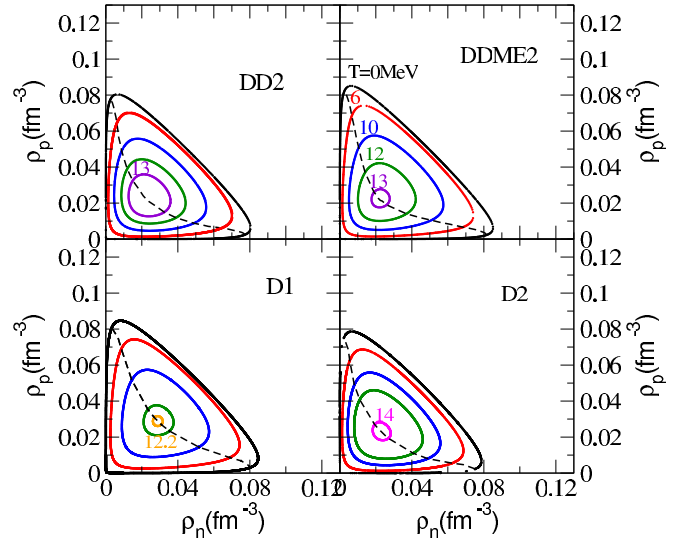


FIG. 5. The spinodal sections on the (ρ_n, ρ_p) plane for DD2 (top left), DDME2 (top right), D1 (bottom left), and D2 (bottom right) at $T = 0, 6, 10,$ and 12 MeV. The smallest unstable regions shown are for $T = 13$ MeV (DD2 and DDME2), 12.2 MeV (D1), and 14 MeV (D2).

same information is given in Fig. 6, where the properties of the critical points (T, ρ_c, y_{pc}) are plotted.

At $T = 0$ MeV, the models SFHx, FSU2R, FSU2H, and TM1e have a proton fraction at the critical point equal to zero or very close to zero. All other models have a similar proton fraction of the order of 0.028 – 0.039 . At $T = 6$ MeV, SFHx, FSU2R, FSU2H, and even TM1e, still present a critical proton fraction of the order of 0.01 or below (for SFHx it is still zero), while for all the other models, it grows up to ≈ 0.09 – 0.11 .

The model SFHx presents a very extreme behavior, keeping a critical proton fraction equal to zero for $T < 10$ MeV, and a critical density of the order of $\approx 0.1 \text{ fm}^{-3}$ for $T < 12$ MeV. The models FSU2H and FSU2R also show a critical proton fraction very close to zero for $T < 8$ MeV. SFHo stands out as being the model that, after SFHx, has the largest critical densities, see Fig. 6 bottom panel. The thermodynamic behavior of these two models will have direct implications in the evolution of core-collapse supernova matter or neutron star mergers since the nonhomogeneous matter will extend to larger densities and larger temperatures. The models SFHx, FSU2R, FSU2H, and TM1e predict clusterization of quite asymmetric matter for quite high temperatures. This will affect the evolution of asymmetric stellar matter as found in neutron star mergers, or core-collapse supernova matter after the neutrino trapped stage.

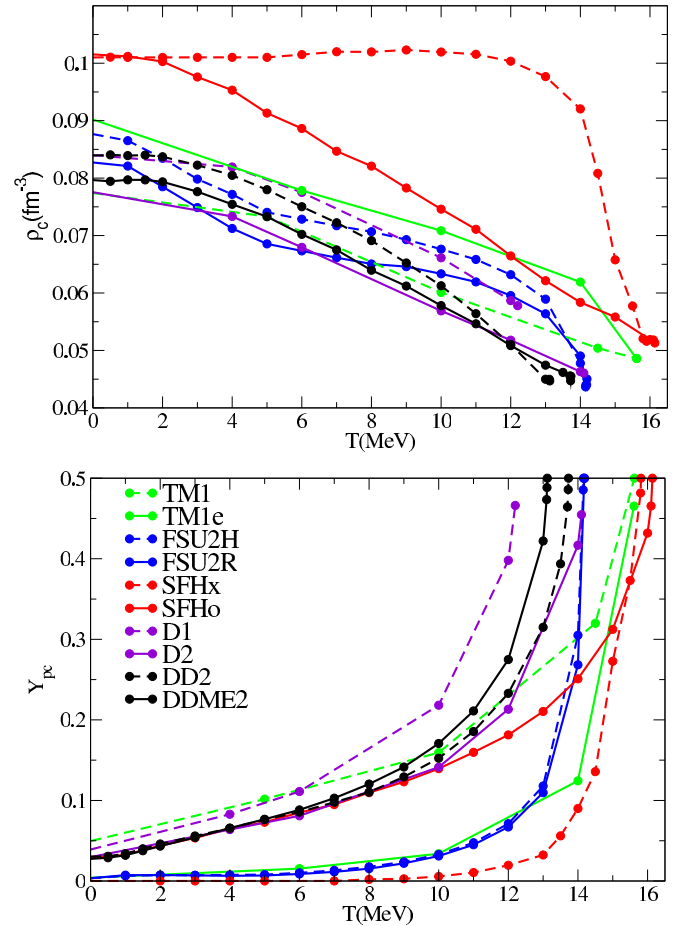
The CEP properties, i.e., the temperature and nuclear matter density and pressure, are given for each model in Table IV. At the CEP, matter is symmetric. The largest CEP temperature, of the order of 16 MeV, is obtained for SFHx and SFHo. D1 presents the smallest CEP temperature of the order of 12 MeV.

In Ref. [21], the authors made a compilation of experimental determinations of the critical temperature of symmetric nuclear matter. The measurements were performed within multifragmentation reactions or fission, and the critical tem-

TABLE III. The critical density ρ_c and the correspondent proton fractions y_{pc} [see Eqs. (28), (29)] for different temperatures and the models considered in this work.

Model	T (MeV)	ρ_c (fm^{-3})	y_{pc}
SFHx	0	0.1010	0.0
SFHo		0.1015	0.0283
FSU2R		0.0827	0.0037
FSU2H		0.0876	0.0022
TM1		0.0774	0.0496
TM1e		0.0902	0.0041
D2		0.0775	0.0296
D1		0.0840	0.0390
DD2		0.0796	0.0302
DDME2		0.0839	0.0274
<hr/>			
SFHx	6	0.1015	0.0
SFHo		0.0886	0.0850
FSU2R		0.0673	0.0083
FSU2H		0.0728	0.0063
TM1e		0.0778	0.0154
D2		0.0679	0.0809
D1		0.0775	0.1110
DD2		0.0702	0.0855
DDME2		0.0750	0.0882
<hr/>			
SFHx	10	0.1019	0.0056
SFHo		0.0746	0.1395
FSU2R		0.0633	0.0304
FSU2H		0.0676	0.0251
TM1		0.0601	0.1594
TM1e		0.0708	0.0339
D2		0.0569	0.1412
D1		0.0661	0.2181
DD2		0.0578	0.1523
DDME2		0.0612	0.1707
<hr/>			
SFHx	14	0.0920	0.09
SFHo		0.0583	0.2509
FSU2R		0.0490	0.2686
FSU2H		0.0477	0.2607
TM1e		0.0619	0.1244
D2		0.0463	0.4167
D1		–	–
DD2		–	–
DDME2		–	–

perature values fluctuate between 15 and 23 MeV. However, some of the estimations are obtained with large uncertainties. The analysis with smaller uncertainties [50] determined a critical temperature of 16.6 ± 0.86 MeV, considering the limiting temperature values obtained in five different mass regions [51], where the authors obtained a temperature above 15 MeV, using both multifragmentation and fission processes. In Ref. [52], the authors used results from six different sets of experimental data, both involving compound nuclei or multifragmentation, and the critical temperature of 17.9 ± 0.4 MeV was obtained. In this last work, the authors also determined the critical density and pressure to be $0.06 \pm 0.01 \text{ fm}^{-3}$, and $0.31 \pm 0.07 \text{ MeV/fm}^3$, respectively. They used Fisher's droplet model, that was modified to account for several ef-


 FIG. 6. The critical density (top) and the critical proton fraction (bottom), as defined in Eq. (29), as a function of the temperature T for some of the models considered in this work.

fects, such as Coulomb, finite-size, or angular momentum effects.

Regarding the models we consider in this study, critical temperatures above 15 MeV are obtained for TM1, TM1e, SFHo, and SFHx. DD models have generally a critical temperature of the order of 14 MeV, or below, and FSU2R and FSU2H have a critical temperature just above 14 MeV.

TABLE IV. The temperatures, and nuclear matter density and pressure at the CEP, for the models considered in this work. At the CEP, the proton fraction is equal to 0.5.

Model	T_c (MeV)	ρ_c (fm^{-3})	P_c (MeV fm^{-3})
SFHx	15.81	0.052	0.242
SFHo	16.14	0.051	0.249
FSU2R	14.19	0.045	0.186
FSU2H	14.16	0.044	0.183
TM1	15.62	0.049	0.239
TM1e	15.61	0.049	0.239
DD2	13.73	0.046	0.178
DDME2	13.12	0.045	0.156
D1	12.22	0.058	0.187
D2	14.14	0.046	0.193

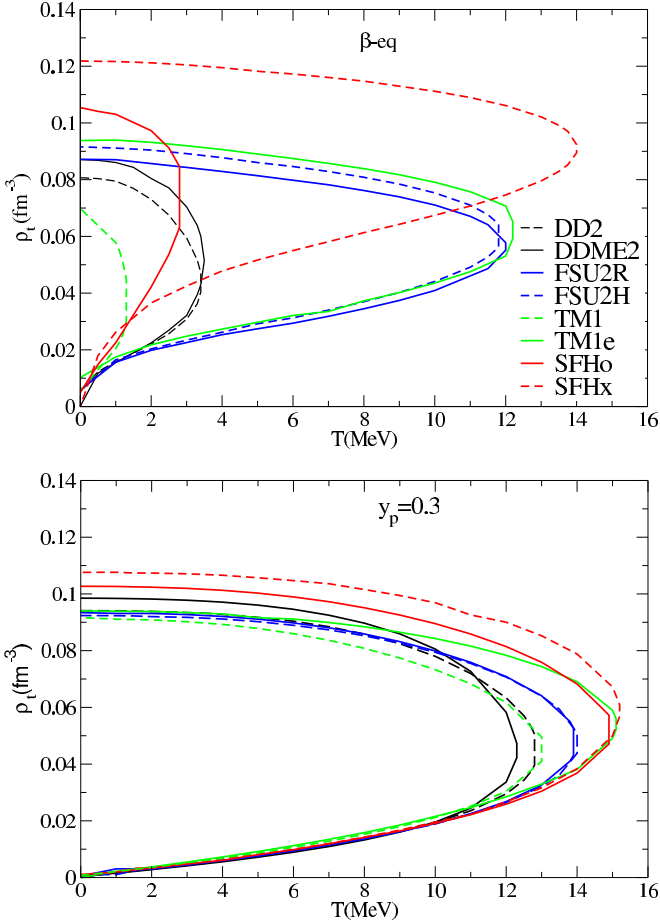


FIG. 7. The transition density, ρ_t , as a function of the temperature for β -equilibrium (top) and fixed proton fraction (bottom) matter for some of the models considered in this work.

Concerning the critical density, all models have a density $\rho_c \gtrsim 0.044 \text{ fm}^{-3}$, but only the models SFHx, SFHo, TM1, TM1e, and D1 predict a density $\gtrsim 0.05 \text{ fm}^{-3}$, as determined in Ref. [52]. SFHx, SFHo, TM1, and TM1e are the models that predict a critical pressure within the range obtained in Ref. [52].

In Ref. [21], the authors have determined the CEP of several RMF models, and, from all the models tested, only the DD models and the models named Z271 predicted a critical temperature above 15 MeV, and the critical pressure and density within the range proposed in Ref. [52]. We should, however, note that the models Z271 predict a maximum stellar mass below $1.7M_\odot$, as shown in Ref. [53].

C. Transition densities

In the following, we discuss the transition densities from nonhomogeneous to homogeneous matter under different proton fraction conditions. In the present work, we estimate the upper and lower density limits of the nonhomogeneous region from the crossing of the y_p line for a fixed proton fraction or the crossing of the $(\rho_p, \rho_n)_{\beta\text{-eq}}$ line with the spinodal section for a given temperature.

In Fig. 7, we show the transition densities as a function of the temperature for two different cases: (i) β -equilibrium;

(ii) a fixed proton fraction of 0.3, a fraction that is representative in core-collapse supernova matter. Inside the represented region, matter is, in principle, nonhomogeneous. This is only an estimation of the instability region, since we are not taking into account finite-size effects.

For $y_p = 0.3$, all models coincide at low densities and temperatures below 10 MeV. At the upper limit, the transition densities take the values $0.1 \pm 0.01 \text{ fm}^{-3}$ at $T = 0$, and up to $T \approx 10 \text{ MeV}$, they decrease $\approx 0.02 \text{ fm}^{-3}$. There exists experimental data that constrain matter with this kind of asymmetry, and they show that the temperature does not affect much the properties of nuclear matter below 10 MeV [25,26,54]. A larger discrepancy is found for temperatures above 10 MeV. The critical temperature for this matter asymmetry varies between 12 and almost 16 MeV, with SFHo and SFHx models giving the largest temperatures, and DD2 and DDME2 the lowest ones.

β -equilibrium matter has a much smaller proton fraction, and there are no experimental data that can constrain the EoS of this kind of matter. Let us, however, recall that all the models satisfy constraints coming from chiral effective field theory calculations for neutron matter. For β -equilibrium matter, we find that the instability region estimated by the models considered vary a lot. SFHx predicts a $T = 0$ transition density above the one obtained for $y_p = 0.3$, and a critical temperature $\approx 14 \text{ MeV}$. Although with more reasonable transition densities at low temperatures, FSU2H and FSU2R also predict very large critical temperatures, $\approx 12 \text{ MeV}$. All the other models predict a critical temperature of the order of 3 MeV, but show a large dispersion on the transition density, with SFHo going above 0.1 fm^{-3} . In Ref. [19], the authors have discussed the influence of the density dependence of symmetry energy on the supernova evolution considering the models TM1 and TM1e. They concluded that there are only minor effects around the core bounce and in the first milliseconds considering the evolution of stars with masses of the order of $12\text{--}15 M_\odot$, precisely because the proton fractions are still not too far from symmetric matter at this stage, and the predictions from both models do not differ much. However, more drastic differences between TM1 and TM1e were found at a later stage, with TM1e giving rise to larger neutrino emissions and a slower decay of the neutrino luminosities.

As referred before, the thermodynamic calculation of the instability regions only allows an estimation of the region where nonhomogeneous matter is expected. Finite-size effects due to the finite range of nuclear force and Coulomb interaction effects will affect the extension of the region of instability, as discussed in Ref. [8]. The authors showed that the transition density obtained from a dynamical spinodal approach would predict transition densities that are $\approx 0.01 \text{ fm}^{-3}$ lower and proton fractions 10% smaller, which are good lower limit estimations, as compared to a thermodynamical spinodal calculation. A Thomas-Fermi calculation of the nonhomogeneous matter may give slightly larger transition densities, as shown in Ref. [10].

It may be of interest to compare the present results on the transition densities with the spinodal calculations mentioned in Sec. I, which also includes the calculation of the pasta structures inside the instability region. These transition

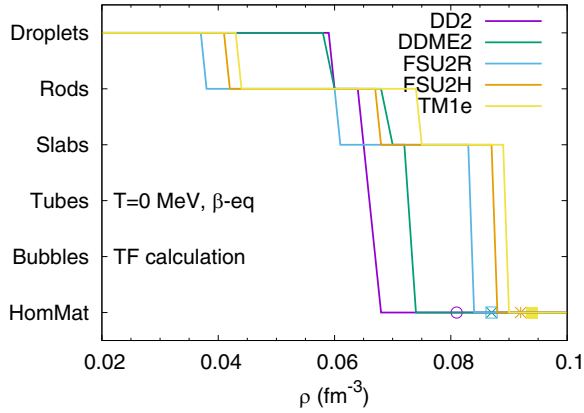


FIG. 8. The different pasta structures from a Thomas-Fermi calculation for cold β -equilibrium matter for some of the models under consideration. The points represent the transition densities from a thermodynamical spinodal calculation given in Table II.

densities, given in Table II, are shown as points in Fig. 8, together with the transition densities between the different nuclear pasta phases, and the transition density to homogeneous matter, for five of the models under consideration, calculated from a Thomas-Fermi approximation at $T = 0$ MeV and β -equilibrium matter [55]. As expected, the crust-core transitions obtained in these calculations are lower than the ones estimated from our thermodynamical approach, by not more than 0.01 fm^{-3} . It is interesting to notice that while DD2 and DDME2 predict a large extension of the spherical clusters in the inner crust, a shorter extension of the rod phase, and no slab phase, or a very narrow one, the models FSU2H, FSU2R, and TM1e predict similar extensions of the droplet-like, rodlike, and slablike pasta structures. These different geometries will certainly affect the transport properties of the neutron star inner crust.

D. Distillation effect

Transport properties are also affected by the proton content of the gas phase, when matter clusterizes. In the following, we determine how the system separates into two phases and the isospin content of each. This will be achieved comparing the direction of the eigenvector of the free energy curvature matrix associated with the negative eigenvalue as defined in Eqs. (23), (24) with the direction defined by $y_p = \rho_p / (\rho_n + \rho_p)$, see Ref. [56]. If the directions are coincident, the instability does not change the proton fraction, and the fluctuations that drive the phase transition are purely density fluctuations. In Ref. [56], it was shown that the eigenvector associated with the instability tends to point in the direction of increasing symmetry of the liquid phase, and, therefore, increasing asymmetry of the gas phase.

We designate by isospin distillation effect the tendency of matter to separate into a low-density phase, the gas phase, that is more neutron rich, i.e., with low proton fraction, and a high-density phase, the clusters, with a proton fraction closer to the one of symmetric matter, i.e., with high proton fraction. A simple way of identifying the distillation effect is by the

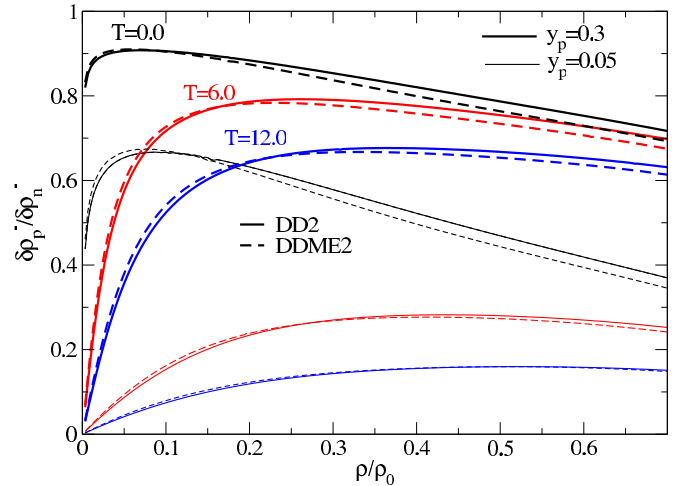


FIG. 9. The fluctuations $\delta\rho_p^-/\delta\rho_n^-$ at $T = 0, 6$, and 12 MeV as function of the density, with $y_p = 0.3$ (thick lines) and 0.05 (thin lines), corresponding to $\rho_p/\rho_n = 0.43$ and 0.05 , for DD2 and DDME2.

comparison of the ratio $\delta\rho_p^-/\delta\rho_n^-$ with ρ_p/ρ_n . This will be used in the following to compare the distillation effect within the models we are discussing.

In Fig. 9, we show the isospin distillation effect for DD2 and DDME2, by plotting the ratio of the proton to the neutron density fluctuations associated with the smallest eigenvalue in the density range $0 < \rho/\rho_0 < 0.7$, where this eigenvalue is essentially negative, but may become positive at the upper limit, as a function of the density, for three temperatures ($T = 0, 6$, and 12 MeV) and two proton fractions, $y_p = 0.05$ and 0.3 , corresponding, respectively, to $\rho_p/\rho_n = 0.05$ and 0.43 . The proton fractions considered are representative of, respectively, cold catalyzed matter in the inner crust [57], and warm matter in protoneutron matter with trapped neutrinos just after the supernova explosion [58]. In Fig. 10, the ratio of the proton to the neutron density is plotted for all the models, for

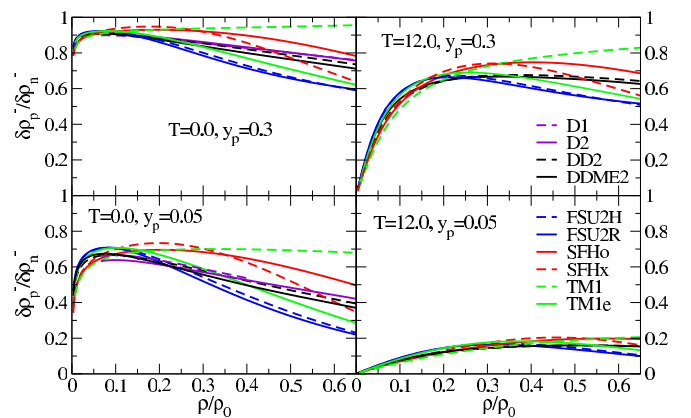


FIG. 10. The fluctuations $\delta\rho_p^-/\delta\rho_n^-$ at $T = 0$ (left panels) and 12 MeV (right panels) as a function of the density, with $y_p = 0.3$ (top panels) and 0.05 (bottom panels), corresponding to $\rho_p/\rho_n = 0.43$ and 0.05 , for FSU2R and FSU2H, SFHo and SFHx, DD2 and DDME2, TM1 and TM1e.

temperatures $T = 0$ and 12 MeV, and the same proton fractions, 0.05 and 0.3.

The higher the ratios, the higher the distillation effect, because the liquid phase becomes proton richer. This effect decreases when the temperature increases, and, except for TM1, it attains a maximum for $0.1 \lesssim \rho/\rho_0 \lesssim 0.3$. The largest differences between models are identified for the proton fraction 0.05 and zero temperature. DD2, DDME2, D1, and D2 all show a very similar behavior in the whole range of densities. In fact, all models have a similar behavior for $\rho/\rho_0 \lesssim 0.2$, and the differences occur above this density. In particular, the ratio of the proton to the neutron density fluctuations for FSU2H and FSU2R (SFHo and SFHx) decreases faster (slower) with the density. For densities around half the saturation density, FSU2H and FSU2R have the smallest distillation effect. These different behaviors reflect the density dependence of the symmetry energy of the models as shown in the top and middle panels of Fig. 1: between $\rho = 0.06$ and 0.1 fm^{-3} , these two models, together with TM1e, have the largest symmetry energy and the smallest symmetry energy slope.

IV. CONCLUSIONS

In the present work, we have studied the instability region of warm and asymmetric nuclear matter, considering several recently proposed calibrated RMF models. At $T = 0$ MeV, these models have been constrained by nuclear properties, *ab initio* theoretical calculations for neutron matter, and neutron star observations. No constraint was imposed at finite temperature. The thermodynamical spinodal sections in the (ρ_p, ρ_n) plane for several temperatures and the critical points have been calculated.

The main conclusions are (i) for symmetric nuclear matter, the transition density to homogeneous matter spreads over a range narrower than 0.01 fm^{-3} , $0.094 < \rho_{\text{sym}} < 0.103 \text{ fm}^{-3}$; (ii) for asymmetric matter, in particular, for $y_p = 0.3$, the transition density to homogeneous matter obtained from the models considered is compatible within $\approx 0.02 \text{ fm}^{-3}$, for temperatures below 8 MeV; (iii) above $T = 8$ MeV, the models differ much more, and the critical temperatures vary in a range of 4 MeV, $12.2 < T_c < 16.2$ MeV; (iv) properties predicted for very asymmetric matter, as β -equilibrated stellar

matter, differ a lot, both on the transition density, and on the critical temperature above which β -equilibrated matter is not clusterized. SFHo, SFHx, FSU2H, and TM1e models predict transition densities from clusterized matter to homogeneous matter for β -equilibrated matter equal or similar to the one for symmetric matter. Since the symmetry energy contribution is a repulsive contribution, one could expect that the extension of the instability region of asymmetric matter would be smaller than the one of symmetric nuclear matter, as it happens with all density-dependent models we have considered. The consequences of this behavior for the evolution of neutrons stars should be understood. It is also interesting to compare the critical temperature of β -equilibrated matter: models SFHx, TM1e, FSU2R, and FSU2H predict a temperature that is just $\lesssim 2$ MeV smaller than the one obtained for symmetric nuclear matter, while all the other models predict temperatures between 8–10 MeV smaller. Again, it is expectable that these properties will have noticeable impact on the the evolution of either a supernova or neutron star mergers.

Sumiyoshi *et al.* [19] have shown, by using two models, TM1 and TM1e [38], which only differ in the isospin channel, that a softer symmetry energy is responsible for a more drastic evolution of the protonneutron star with larger neutrino emissions, giving rise to higher neutrino luminosities and average energies. Also, very recently, the SFHo EoS has been used in several simulations of neutron star mergers, black hole-neutron star (BH-NS) mergers and core-collapse supernova [59–62]. In particular, in Ref. [60], the authors have discussed the possibility of a kilonova production during a BH-NS merger using several EoS. Among these models, SFHo predicted the smallest fractions of mass in the disk and ejecta, i.e., the smaller mass fractions outside the black hole.

ACKNOWLEDGMENTS

This work was partly supported by the FCT (Portugal) Projects No. UID/FIS/04564/2019, No. UID/FIS/04564/2020, and No. POCI-01-0145-FEDER-029912, and by PHAROS COST Action CA16214. H.P. acknowledges the grant CEECIND/03092/2017 (FCT, Portugal). S.A. acknowledges the HGS-HIRE Abroad grant from Helmholtz Graduate School for Hadron and Ion Research.

-
- [1] M. Oertel, M. Hempel, T. Klöhn, and S. Typel, *Rev. Mod. Phys.* **89**, 015007 (2017).
 - [2] M. Sinha and A. Sedrakian, *Phys. Rev. C* **91**, 035805 (2015); Ad. R. Raduta, A. Sedrakian, and F. Weber, *Mon. Not. R. Astron. Soc.* **475**, 4347 (2018); R. Negreiros, L. Tolos, M. Centelles, A. Ramos, and V. Dexheimer, *Astrophys. J.* **863**, 104 (2018); M. Fortin, G. Taranto, F. G. Burgio *et al.*, *Mon. Not. R. Astron. Soc.* **475**, 5010 (2018); J. Torres Patiño, E. Bauer, and I. Vidaña, *Phys. Rev. C* **99**, 045808 (2019).
 - [3] R. Fernández and B. D. Metzger, *Mon. Not. R. Astron. Soc.* **435**, 502 (2013).
 - [4] O. Just, A. Bauswein, R. A. Pulpillo, S. Gorieli, and H.-T. Janka, *Mon. Not. R. Astron. Soc.* **448**, 541 (2014).
 - [5] S. Rosswog, *Int. J. Mod. Phys. D* **24**, 1530012 (2015).
 - [6] H. Müller and B. D. Serot, *Phys. Rev. C* **52**, 2072 (1995).
 - [7] C. Providência, L. Brito, S. S. Avancini, D. P. Menezes, and Ph. Chomaz, *Phys. Rev. C* **73**, 025805 (2006).
 - [8] C. Ducoin, J. Margueron, C. Providência, and I. Vidaña, *Phys. Rev. C* **83**, 045810 (2011).
 - [9] C. Ducoin, C. Providência, A. M. Santos, L. Brito, and Ph. Chomaz, *Phys. Rev. C* **78**, 055801 (2008).
 - [10] S. S. Avancini, S. Chiacchiera, D. P. Menezes, and C. Providência, *Phys. Rev. C* **82**, 055807 (2010); **85**, 059904(E) (2012).
 - [11] Ph. Chomaz, M. Colonna, and J. Randrup, *Phys. Rep.* **389**, 263 (2004).

- [12] S. S. Avancini, D. P. Menezes, M. D. Alloy, J. R. Marinelli, M. M. W. Moraes, and C. Providência, *Phys. Rev. C* **78**, 015802 (2008).
- [13] D. G. Ravenhall, C. J. Pethick, and J. R. Wilson, *Phys. Rev. Lett.* **50**, 2066 (1983).
- [14] H. Sonoda, G. Watanabe, K. Sato, K. Yasuoka, and T. Ebisuzaki, *Phys. Rev. C* **77**, 035806 (2008); **81**, 049902(E) (2010).
- [15] M. Hempel and J. Schaffner-Bielich, *Nucl. Phys. A* **837**, 210 (2010).
- [16] A. R. Raduta and F. Gulminelli, *Phys. Rev. C* **82**, 065801 (2010).
- [17] J. M. Lattimer and F. D. Swesty, *Nucl. Phys. A* **535**, 331 (1991).
- [18] H. Shen, H. Toki, K. Oyamatsu, and K. Sumiyoshi, *Nucl. Phys. A* **637**, 435 (1998).
- [19] K. Sumiyoshi, K. Nakazato, H. Suzuki, J. Hu, and H. Shen, *Astrophys. J.* **887**, 110 (2019).
- [20] S. S. Avancini, M. Ferreira, H. Pais, C. Providência, and G. Röpke, *Phys. Rev. C* **95**, 045804 (2017).
- [21] O. Lourenço, M. Dutra, and D. P. Menezes, *Phys. Rev. C* **95**, 065212 (2017).
- [22] H. Pais, R. Bougault, F. Gulminelli, C. Providência *et al.*, *Phys. Rev. Lett.* **125**, 012701 (2020).
- [23] H. Pais, F. Gulminelli, C. Providência, and G. Röpke, *Phys. Rev. C* **97**, 045805 (2018).
- [24] S. Typel, G. Röpke, T. Klähn, D. Blaschke, and H. H. Wolter, *Phys. Rev. C* **81**, 015803 (2010).
- [25] R. Bougault *et al.*, *J. Phys. G* **47**, 025103 (2020).
- [26] L. Qin, K. Hagel, R. Wada, J. B. Natowitz, S. Shlomo, A. Bonasera, G. Röpke, S. Typel, Z. Chen, M. Huang *et al.*, *Phys. Rev. Lett.* **108**, 172701 (2012).
- [27] T. Custódio, A. Falcão, H. Pais, C. Providência, F. Gulminelli, and G. Röpke, *Eur. Phys. J. A* **56**, 295 (2020).
- [28] S. S. Avancini, L. Brito, Ph. Chomaz, D. P. Menezes, and C. Providência, *Phys. Rev. C* **74**, 024317 (2006).
- [29] M. Beiner, H. Flocard, N. Van Giai, and P. Quentin, *Nucl. Phys. A* **238**, 29 (1975).
- [30] N. Alam, H. Pais, C. Providência, and B. K. Agrawal, *Phys. Rev. C* **95**, 055808 (2017).
- [31] M. B. Tsang, J. R. Stone, F. Camera *et al.*, *Phys. Rev. C* **86**, 015803 (2012).
- [32] A. Bauswein, N.-U. F. Bastian, D. B. Blaschke, K. Chatziioannou, J. A. Clark, T. Fischer, and M. Oertel, *Phys. Rev. Lett.* **122**, 061102 (2019).
- [33] A. W. Steiner, M. Hempel, and T. Fischer, *Astrophys. J.* **774**, 17 (2013).
- [34] T. Fischer, N.-U. Bastian, D. Blaschke, M. Cierniak, M. Hempel *et al.*, *Publ. Astron. Soc. Austral.* **34**, 67 (2017).
- [35] L. Tolos, M. Centelles, and A. Ramos, *Pub. Astron. Soc. Aust.* **34**, e065 (2017).
- [36] L. Tolos, M. Centelles, and A. Ramos, *Astrophys. J.* **834**, 3 (2017).
- [37] Y. Sugahara and H. Toki, *Nucl. Phys. A* **579**, 557 (1994).
- [38] H. Shen, F. Ji, J. Hu, and K. Sumiyoshi, *Astrophys. J.* **891**, 148 (2020).
- [39] G. A. Lalazissis, T. Niksić, D. Vretenar, and P. Ring, *Phys. Rev. C* **71**, 024312 (2005).
- [40] S. Antic and S. Typel, *Nucl. Phys. A* **938**, 92 (2015).
- [41] M. Modell and R. C. Reid, *Thermodynamics and Its Applications*, 2nd ed. (Prentice-Hall, Englewood Cliffs, 1983).
- [42] M. Hempel (private communication).
- [43] P. B. Demorest, T. Pennucci, S. M. Ransom, M. S. E. Roberts, and J. W. T. Hessels, *Nature (London)* **467**, 1081 (2010); J. Antoniadis *et al.*, *Science* **340**, 6131 (2013).
- [44] T. E. Riley, A. L. Watts, S. Bogdanov, P. S. Ray *et al.*, *Astrophys. J. Lett.* **887**, L21 (2020); M. C. Miller, F. K. Lamb, A. J. Bogdanov, Z. Arzoumanian *et al.*, *ibid.* **887**, L24 (2020).
- [45] I. Tews, J. M. Lattimer, A. Ohnishi, and E. Kolomeitsev, *Astrophys. J.* **848**, 105 (2017).
- [46] J. Birkhan, M. Miorelli, S. Bacca *et al.*, *Phys. Rev. Lett.* **118**, 252501 (2017).
- [47] S. Hama, B. C. Clark, E. D. Cooper, H. S. Sherif, and R. L. Mercer, *Phys. Rev. C* **41**, 2737 (1990); E. D. Cooper, S. Hama, B. C. Clark, and R. L. Mercer, *ibid.* **47**, 297 (1993).
- [48] K. Hebeler, J. M. Lattimer, C. J. Pethick, and A. Schwenk, *Astrophys. J.* **773**, 11 (2013).
- [49] D. Vautherin and D. M. Brink, *Phys. Rev. C* **5**, 626 (1972).
- [50] J. B. Natowitz, K. Hagel, Y. Ma, M. Murray, L. Qin, R. Wada, and J. Wang, *Phys. Rev. Lett.* **89**, 212701 (2002).
- [51] V. A. Karnaukhov, *Phys. At. Nucl.* **71**, 2067 (2008).
- [52] J. B. Elliott, P. T. Lake, L. G. Moretto, and L. Phair, *Phys. Rev. C* **87**, 054622 (2013).
- [53] H. Pais and C. Providência, *Phys. Rev. C* **94**, 015808 (2016).
- [54] J. Pochodzalla *et al.*, *Phys. Rev. Lett.* **75**, 1040 (1995).
- [55] F. Grill, H. Pais, C. Providência, I. Vidaña, and S. S. Avancini, *Phys. Rev. C* **90**, 045803 (2014).
- [56] J. Margueron and P. Chomaz, *Phys. Rev. C* **67**, 041602(R) (2003).
- [57] F. Grill, C. Providência, and S. S. Avancini, *Phys. Rev. C* **85**, 055808 (2012).
- [58] M. Prakash, I. Bombaci, M. Prakash, P. J. Ellis, J. M. Lattimer, and G. E. Brown, *Phys. Rept.* **280**, 1 (1997).
- [59] C. Barbieri, O. S. Salafia, M. Colpi, G. Ghirlanda, A. Perego, and A. Colombo, *Astrophys. J.* **887**, L35 (2019).
- [60] C. Barbieri, O. S. Salafia, A. Perego, M. Colpi, and G. Ghirlanda, *Eur. Phys. J. A* **56**, 8 (2020).
- [61] J. R. Westernacher-Schneider, E. O'Connor, E. O'Sullivan, I. Tamborra, M.-R. Wu, S. M. Couch, and F. Malmenbeck, *Phys. Rev. D* **100**, 123009 (2019).
- [62] J. M. Miller, B. R. Ryan, J. C. Dolence, A. Burrows, C. J. Fontes, C. L. Fryer, O. Korobkin, J. Lippuner, M. R. Mumpower, and R. T. Wollaeger, *Phys. Rev. D* **100**, 023008 (2019).